1990

Prediction of Cascade Performance Using an Incompressible Navier-Stokes Technique

Hobson, G.V.; Lakshminarayana, B.

ASME

Hobson, G. V., and B. Lakshminarayana. "Prediction of cascade performance using an incompressible Navier-Stokes technique." ASME 1990 International Gas Turbine and Aeroengine Congress and Exposition. American Society of Mechanical Engineers, 1990.

http://hdl.handle.net/10945/61955

THE AMERICAN SOCIETY OF MECHANICAL ENGINEERS
345 E. 47 St., New York, N.Y. 10017

90-GT-261

Prediction of Cascade Performance Using an Incompressible Navier-Stokes Technique

G. V. HOBSON and B. LAKSHMINARAYANA
Department of Aerospace Engineering
Pennsylvania State University
153 Hammond Building
University Park, PA 16801

ABSTRACT

A fully elliptic, control volume solution of the two-dimensional incompressible Navier-Stokes equations for the prediction of cascade performance over a wide incidence range is presented in this paper. The numerical technique is based on a new pressure substitution method. A Poisson equation is derived from the pressure weighted substitution of the full momentum equations into the continuity equation. The analysis of a double circular arc compressor cascade is presented, and the results are compared with the available experimental data at various incidence angles. Good agreement is obtained for the blade pressure distribution, boundary layer and wake profiles, skin friction coefficient, losses and outlet angles. Turbulence effects are simulated by the Low-Reynolds-Number version of the k-ϵ turbulence model.

NOMENCLATURE

A = discretization coefficient.
B = pressure gradient coefficient.
C = pressure gradient coefficient.
C_f = skin friction coefficient, $\frac{\tau_w}{\frac{1}{2}(\rho w_i^2)}$.
C_L = lift coefficient.
C_p = pressure coefficient, $\frac{p_i - p_l}{\frac{1}{2}(\rho w_i^2)}$.
$C_\mu, C_{\epsilon 1}, C_{\epsilon 2}$ = empirical constants in the turbulence model.
f_μ, f_1, f_2 = empirical functions in the turbulence model.
G_1, G_2 = contravariant velocity components.
J = Jacobian of the transformation.
k = turbulent kinetic energy.
L_i = inlet turbulence length scale.
L_2 = norm, sum of the moduli of the errors.
n = distance normal to blade surface.
p = static pressure.
p_T = total pressure.
P = production of turbulent kinetic energy.
Re_y, Re_t = turbulent Reynolds numbers.
S = source term.
Tu = turbulence intensity, $\left[(\overline{u'})^2\right]^{1/2}/u$.
u = axial velocity.
v = tangential velocity.
w = total velocity component.
x = axial direction normalized by blade chord length in the physical domain.
y = tangential direction normalized by blade chord in the physical domain.
α = transformation coefficient, angle of incidence.
β = transformation coefficient.
δ_o = outlet flow deviation angle.
ϵ = dissipation rate.
γ = transformation coefficient.
Γ = diffusion coefficient.
μ = molecular viscosity.
μ_t = turbulent (eddy) viscosity.
ϕ = dependent variable.
Φ = dissipation function.
ρ = density.
$\sigma_k, \sigma_\epsilon$ = empirical constants in turbulence model.
τ_w = wall shear stress, $\mu \left.\frac{\partial u}{\partial y}\right|_{wall}$.

*Presented at the Gas Turbine and Aeroengine Congress and Exposition—June 11-14, 1990—Brussels, Belgium
This paper has been accepted for publication in the Transactions of the ASME
Discussion of it will be accepted at ASME Headquarters until September 30, 1990

$\bar{\omega}$ = total pressure loss coefficient, $(p_{T_i} - p_{T_o})/(\rho w_i^2/2)$.
ξ = streamwise coordinate, computational domain.
η = cross-stream direction, computational domain.

Superscripts

ϕ = dependent variable.
m = iteration counter.
u = axial momentum equation coefficient.
v = tangential momentum equation coefficient.

Subscripts

i = inlet station.
l = local values.
n,e,s,w = control volume faces.
N,E,S,W = grid points, at compass locations.
o = outlet station.
O = central grid point.
P = pressure.
T = stagnation quantity.
U = cross derivative terms.

INTRODUCTION

A fully elliptic calculation of steady internal flows is essential in order that regions of pressure ellipticity and streamwise diffusion can be accurately resolved. The resolution of these elliptic regions is essential for the numerical simulation of flow past airfoils and cascades that are operating at, or close to, their optimum condition, which could entail some regions of flow separation.

In flows where there is such strong viscid-inviscid interaction, it is essential that the full Navier-Stokes equations be solved. When compared with the parabolic marching technique as proposed by Pouagare and Lakshminarayana (1985), the method described below is not computationally efficient. The Pressure-based method have recently been shown by Abdallah (1989) to be computationally more efficient than the artificial compressibility method. With the current increase in computer speeds, this type of computation can be justified. The most important justification for elliptic techniques is that physical phenomena, including viscid-inviscid flow interactions, separated flow regions and pressure distributions, are accurately resolved.

The computational procedure developed in this paper is based on the original Navier-Stokes solution method developed by Caretto, Gossman, Patankar and Spalding (1972). The original SIMPLE or pressure correction method (PCM) algorithm suffered severely from geometrical limitations because the equations were written in Cartesian coordinates and the staggered grid arrangement utilized did not enable easy transformation of the equations into generalized coordinates. The pressure correction method requires the solution of a Poisson pressure correction equation and a subsequent explicit correction of the velocity and pressure field. Rhie and Chow (1983), who proposed the pressure weighted method (PWM), were the first to compute on a regular, or nonstaggered grid. This was achieved by substituting the full momentum equations into the integral form of the continuity equation. Their solution procedure, however, still relied on the basic SIMPLE or pressure correction algorithm. Hah (1984) and Davis, et al. (1988) provided cascade viscous flow solutions using, respectively, relaxation and time marching techniques. Both formulations were for compressible flow; however, Hah computed incompressible flow.

The new pressure substitution method (PSM), developed and utilized in this paper, permits the solution of the static pressure and allows for a direct coupling of the momentum and pressure equations to be solved in block form. Three different formulations with nonstaggered grids have been suggested by Shih and Ren (1984). Some of these employ the Poisson equation for pressure in place of the continuity equation. Their formulation was derived in non-conservative, finite difference form in contrast to the derivation of the equations in conservative form in the present study. Thus, the code developed in this paper uses pressure weighting to allow the solution of the discretized equations on a regular grid, and the equations are coupled by the substitution of the pressure weighted form of the momentum equations into the integral form of the continuity equation.

A refined turbulence model has been incorporated into this procedure, which is an extension of the widely used $k-\epsilon$ model as proposed by Launder and Spalding (1974). The effects of turbulence are simulated by the Low-Reynolds-Number version of the $k-\epsilon$ turbulence model as proposed by Lam and Bremhorst (1981). Rodi and Scheuerer (1985) used a similar extended version of the $k-\epsilon$ equations, but with a boundary layer procedure which was valid for flows without separation. The extensions entail the simulation of viscous and near wall effects, and laminar to turbulent flow transition, and in particular its dependence on the freestream turbulence intensity.

The original contribution of this paper is the development of a new pressure substitution method which is more efficient than the pressure correction method. The fully validated code, proposed by Hobson (1989), is used in a simulation mode to carry out a parameteric study of cascade flows. The objective of the paper is to demonstrate the capability of a Navier-Stokes code to capture the entire flowfield, including loses, wake and boundary layer profiles, and the extent of flow separation. Most importantly, the code is utilized to understand the effect of free stream turbulence and incidence angle on cascade performance.

THEORETICAL FORMULATION

Mathematical Model

The equations governing two-dimensional incompressible flow are the continuity equation,

$$\frac{\partial}{\partial x}(\rho u)+\frac{\partial}{\partial y}(\rho v)=0 \qquad [1]$$

and the general form of the conservation equation for momentum.

$$\frac{\partial}{\partial x}(\rho u\phi)+\frac{\partial}{\partial y}(\rho v\phi)=\frac{\partial}{\partial x}\left[\Gamma^{\phi}\frac{\partial \phi}{\partial x}\right]+\frac{\partial}{\partial y}\left[\Gamma^{\phi}\frac{\partial \phi}{\partial y}\right]+S^{\phi} \qquad [2]$$

In the above two equations, ρ is the fluid density and u and v are the velocities in the x and y directions respectively as shown in Fig. 1.

For the dependent variables, ϕ, to be solved the diffusion constants and source terms, are as follows.

Conservation Equation	ϕ	Γ^{ϕ}	S^{ϕ}
x-Momentum	u	$\mu+\mu_t$	$-\frac{\partial p}{\partial x}$
y-Momentum	v	$\mu+\mu_t$	$-\frac{\partial p}{\partial y}$
Turbulent Kinetic Energy	k	$\mu+\frac{\mu_t}{\sigma_k}$	$P-\rho\epsilon$
Turbulent Dissipation	ϵ	$\mu+\frac{\mu_t}{\sigma_\epsilon}$	$\frac{\epsilon}{k}\left[C_{\epsilon 1}f_1 P-C_{\epsilon 2}f_2\rho\epsilon\right]$

[3]

In the above table, μ is the dynamic viscosity, p is the static pressure, k the turbulent kinetic energy, and ϵ the rate of dissipation of turbulent kinetic energy.

The eddy viscosity, μ_t, is related to the turbulent kinetic energy k and the rate of dissipation ϵ by

$$\mu_t=\rho C_\mu f_\mu \frac{k^2}{\epsilon} \qquad [4]$$

where C_μ is an empirical constant and f_μ a function which expresses viscous and near-wall effects on the eddy viscosity. The function f_μ, given by Lam and Bremhorst (1981), reads

$$f_\mu=\left[1-\exp(-0.0165Re_y)\right]^2\left[1+\frac{20.5}{Re_t}\right] \qquad [5]$$

where the turbulent Reynolds numbers Re_y and Re_t are defined as

$$Re_y=\frac{\sqrt{k}y\rho}{\mu}\ ;\ Re_t=\frac{k^2\rho}{\epsilon\mu} \qquad [6]$$

The term Φ is defined as

$$\Phi=2\left\{\left[\frac{\partial u}{\partial x}\right]^2+\left[\frac{\partial v}{\partial y}\right]^2+\left[\frac{\partial v}{\partial x}\frac{\partial u}{\partial y}\right]\right\}+\left[\frac{\partial u}{\partial y}\right]^2+\left[\frac{\partial v}{\partial x}\right]^2 \qquad [7]$$

and the production, P, of turbulent kinetic energy, k, is:

$$P=\mu_t\Phi \qquad [8]$$

The empirical low-Reynolds number functions f_1 and f_2 appearing in the ϵ-equation are:

$$f_1=1+\left[\frac{0.06}{f_\mu}\right]^3\ ;\quad f_2=1-\exp(-Re_t^2) \qquad [9]$$

For the remaining empirical constants, the standard values cited by Rodi and Scheuerer (1985) have been used: $C_\mu=0.09$, $C_{\epsilon 1}=1.44$, $C_{\epsilon 2}=1.92$, $\sigma_k=1.0$, and $\sigma_\epsilon=1.3$.

Transformation of the Basic Equation

Equations [1] and [2] are transformed into generalized coordinates ξ,η by the general transformation $\xi=\xi(x,y)$ and $\eta=\eta(x,y)$. The transformed equations are:

$$\frac{\partial}{\partial \xi}(\rho G_1)+\frac{\partial}{\partial \eta}(\rho G_2)=0 \qquad [10]$$

and

$$\frac{\partial}{\partial \xi}(\rho G_1\phi)+\frac{\partial}{\partial \eta}(\rho G_2\phi)=\frac{\partial}{\partial \xi}\left\{\frac{\Gamma^{\phi}}{J}\left[\alpha\frac{\partial \phi}{\partial \xi}-\beta\frac{\partial \phi}{\partial \eta}\right]\right\}+\frac{\partial}{\partial \eta}\left\{\frac{\Gamma^{\phi}}{J}\left[\gamma\frac{\partial \phi}{\partial \eta}-\beta\frac{\partial \phi}{\partial \xi}\right]\right\}+S^{\phi}J \qquad [11]$$

where

$$G_1=u\frac{\partial y}{\partial \eta}-v\frac{\partial x}{\partial \eta};\qquad G_2=v\frac{\partial x}{\partial \xi}-u\frac{\partial y}{\partial \xi} \qquad [12]$$

and

$$\alpha=\left[\frac{\partial x}{\partial \eta}\right]^2+\left[\frac{\partial y}{\partial \eta}\right]^2;\quad \beta=\frac{\partial x}{\partial \xi}\frac{\partial x}{\partial \eta}+\frac{\partial y}{\partial \xi}\frac{\partial y}{\partial \eta}$$
$$\gamma=\left[\frac{\partial x}{\partial \xi}\right]^2+\left[\frac{\partial y}{\partial \xi}\right]^2;\quad J=\frac{\partial x}{\partial \xi}\frac{\partial y}{\partial \eta}-\frac{\partial x}{\partial \eta}\frac{\partial y}{\partial \xi} \qquad [13]$$

G_1 and G_2 are directly related to the contravariant velocity components and J is the Jacobian of the transformation.

Discretization of the Transport Equations

Equations [10] and [11] are integrated over the control volume as shown in Fig.1.

$$[\rho G_1]_w^e+[\rho G_2]_s^n=0 \qquad [14]$$

$$\left\{(\rho G_1\phi)-\frac{\Gamma^\phi}{J}\left[\alpha\frac{\partial\phi}{\partial\xi}\right]\right\}_w^e+\left\{(\rho G_2\phi)-\frac{\Gamma^\phi}{J}\left[\gamma\frac{\partial\phi}{\partial\eta}\right]\right\}_s^n=$$

$$-\left\{\frac{\Gamma^\phi}{J}\left[\beta\frac{\partial\phi}{\partial\eta}\right]_w^e+\frac{\Gamma^\phi}{J}\left[\beta\frac{\partial\phi}{\partial\xi}\right]_s^n\right\}+S^\phi J \qquad [15]$$

where n, s, e and w are the locations of the intersection between the control volume faces and the grid lines.

The discretized form of the continuity equation [14] will be dealt with in the next section. Equation [15] will be now be fully discretized.

In the present scheme, all properties are defined at the nodes O, N, S, E and W. Thus the following general approximations are made for the above finite difference expressions on the left-hand side of Equation [15].

$$[\rho G_1\phi]_e\approx[\rho G_1]_e\ \frac{1}{2}\left[\phi_O+\phi_E\right]$$

$$\left\{\frac{\Gamma^\phi}{J}\left[\alpha\frac{\partial\phi}{\partial\xi}\right]\right\}_e\approx\left[\frac{\Gamma^\phi}{J}\alpha\right]_e\left[\frac{\phi_O-\phi_E}{\Delta\xi}\right] \qquad [16]$$

Quantities such as $[\rho G_1]_e$ and $[\Gamma^\phi\alpha/J]_e$ are obtained by linear interpolation in the computational plane. Similar forms of equation [16] are substituted into [15] which results in a relationship between ϕ_o and the neighboring values:

$$A_O^\phi\phi_O=A_N^\phi\phi_N+A_S^\phi\phi_S+A_E^\phi\phi_E+A_W^\phi\phi_W+S_U^\phi+S_P^\phi J \qquad [17]$$

or

$$A_O^\phi\phi_O=\sum A_i^\phi\phi_i+S_U^\phi+S_P^\phi J \qquad [18]$$

where S_U^ϕ which contains the cross derivative terms is the first term on the right-hand side of [15]. The A_i^ϕ,s contain the convection and diffusion terms as given by the coefficients on the right-hand side of equation [16].

S_P^ϕ contains the pressure gradient terms:

$$\phi=u;\quad S_P^u=-B^u\frac{\partial p}{\partial\xi}-C^u\frac{\partial p}{\partial\eta}$$

$$\phi=v;\quad S_P^v=-B^v\frac{\partial p}{\partial\xi}-C^v\frac{\partial p}{\partial\eta} \qquad [19]$$

where:

$$B^u=\frac{\frac{\partial y}{\partial\eta}}{A_O};\quad C^u=-\frac{\frac{\partial y}{\partial\xi}}{A_O}$$

$$B^v=-\frac{\frac{\partial x}{\partial\eta}}{A_O};\quad C^v=\frac{\frac{\partial x}{\partial\xi}}{A_O} \qquad [20]$$

A_O^ϕ is the sum of all the A_i^ϕ,s at the N,S,E and W points. These coefficients are modified according to the hybrid differencing scheme proposed by Spalding (1972). The transformation is such that $\Delta\xi=\Delta\eta=1$ and as such all multiples of these terms have been neglected.

Pressure Substitution Method

The method will be explained by neglecting such scalar quantities as temperature and the turbulence quantities. For simplicity the explanation of the method will be restricted to rectangular Cartesian coordinates.

The implicit, discretized u- and v-momentum equations at node O in Cartesian coordinates is derived from [18] and [19]

$$u_O^{m+1}=\sum A_i^u u_i^{m+1}-B^u\frac{\partial p}{\partial x}^m$$

$$v_O^{m+1}=\sum A_i^v v_i^{m+1}-C^v\frac{\partial p}{\partial y}^m \qquad [21]$$

where the all the coefficients on the right-hand side have been divided by A_O^ϕ.

A Poisson pressure equation is to be derived from the combined continuity and momentum equations. Consider the integral form of equation [1] and not equation [14].

$$[\rho u]_w^e+[\rho v]_s^n=0 \qquad [22]$$

It is assumed that a new set of velocities u^{m+1} and v^{m+1} are obtained from equation [21], where the superscript m denotes the initial guess and the superscript m+1 denotes the new implicit solution of the relevant variable. In general, u^{m+1} and v^{m+1} will not satisfy the continuity equation; instead, a net mass source is produced. This derivation of the net source is now presented.

When considering equation [22], it is noted that u is to be evaluated at station e, but this must be determined from values at stations E and O as shown in Fig. 1. These values are determined from the following relationships,

$$u_E^{m+1}=\sum A_i^u u_i^{m+1}\Big|_E - B_E^u \frac{\partial p^m}{\partial x}\Big|_E \qquad [23]$$

$$u_O^{m+1}=\sum A_i^u u_i^{m+1}\Big|_O - B_O^u \frac{\partial p^m}{\partial x}\Big|_O \qquad [24]$$

$$u_e^{m+1}=\sum A_i^u u_i^{m+1}\Big|_e - B_e^u \frac{\partial p^m}{\partial x}\Big|_e \qquad [25]$$

The following two assumptions are now made with regard the first term on the right hand side of equation [25] and the coefficient of the last term of the same equation, i.e., assume:

$$\sum A_i^u u_i^{m+1}\Big|_e = \frac{1}{2}\left[\sum A_i^u u_i^{m+1}\Big|_O + \sum A_i^u u_i^{m+1}\Big|_E\right]$$

$$B_e^u = \frac{1}{2}\left[B_O^u + B_E^u\right] \qquad [26]$$

Upon substitution of the rearranged forms of equations [23] and [24] and equation [26] into equation [25], the following equation results.

$$u_e^{m+1}=\frac{1}{2}\left\{\left[u_E^{m+1}+u_O^{m+1}\right]+\left[B_O^u \frac{\partial p^m}{\partial x}\Big|_O + B_E^u \frac{\partial p^m}{\partial x}\Big|_E\right] - (B_O^u+B_E^u)\frac{\partial p^m}{\partial x}\Big|_e\right\} \qquad [27]$$

or

$$u_e^{m+1}=\bar{u}_e^{m+1}+\frac{1}{2}\left[B_O^u \frac{\partial p^m}{\partial x}\Big|_O + B_E^u \frac{\partial p^m}{\partial x}\Big|_E\right] - B_e^u \frac{\partial p^m}{\partial x}\Big|_e \qquad [28]$$

where

$$\bar{u}_e^{m+1}=\frac{1}{2}\left[u_E^{m+1}+u_O^{m+1}\right] \qquad [29]$$

Similar equations can be derived for u_w^{m+1}, u_n^{m+1} and u_s^{m+1}. Equation [28] and its derivation is referred to as the presssure weighted method (PWM). This was first introduced by Rhie and Chow (1984), who found a similar form to be effective in coupling the momentum and continuity equations. Let u_e^* be equal to the first three terms on the right-hand side of [28], i.e.,

$$u_e^*=\bar{u}_e^{m+1}+\frac{1}{2}\left[B_O^u \frac{\partial p^m}{\partial x}\Big|_O + B_E^u \frac{\partial p^m}{\partial x}\Big|_E\right] \qquad [30]$$

The assumption is made that the following form of the continuity equation is satisfied:

$$[\rho u^{m+1}]_w^e + [\rho v^{m+1}]_s^n = 0 \qquad [31]$$

This is the ultimate converged solution that is sought. Most researchers, such as Caretto et al. (1972), Rhie and Chow (1983), and Hah (1984), now invoke the pressure correction method (PCM) and solve a pressure correction (p') equation. Then, the intermediate velocity field and the previous pressure field are updated by the gradient of the pressure correction and the actual pressure correction respectively. This explicit correction step is neglected in the present work, with no detrimental effect. In most test cases, this procedure showed better convergence behavior than the original PCM procedure.

Upon substitution of equation [27], and similar forms of it for u_w^{m+1}, u_n^{m+1} and u_s^{m+1}, into equation [30] the following pressure equation results:

$$-\rho B_e^u \frac{\partial p}{\partial x}\Big|_e + \rho B_w^u \frac{\partial p}{\partial x}\Big|_w - \rho C_n^v \frac{\partial p}{\partial y}\Big|_n + \rho C_s^v \frac{\partial p}{\partial y}\Big|_s = S_P^m \qquad [32]$$

In discretized form, the implicit pressure equation is

$$A_O^p p_O^{m+1} = A_N^p p_N^{m+1} + A_S^p p_S^{m+1} + A_E^p p_E^{m+1} + A_W^p p_W^{m+1} + S_P^m \qquad [33]$$

where the coefficients A_i^p are determined from [32].

The source term of equation [32] is

$$S_P^m = \left[\rho u^*\right]_w^e + \left[\rho v^*\right]_s^n \qquad [34]$$

where u^* and v^* are of the form of equation [29].

The major difference between this derivation and that of Rhie and Chow (1984) is evident when one considers equation [29]. The present method does not include a pressure gradient term at the control volume face for the solution of the pressure equation [32]. The Shih and Ren (1984) formulation, which was non-conservative, did not include the pressure weighted method. In comparison with the pressure weighted method, which includes dissipation dependent on the pressure gradient, their pressure equation only has velocity gradients in the source term.

The extension of this algorithm to generalized coordinates is similar to the formulation presented by Rhie and Chow (1984).

Boundary Conditions

The inlet flow conditions are specified, and at the exit plane (which is at least two chord lengths downstream of the cascade) the streamwise derivative of all the solution variables is set equal to zero. No-slip boundary conditions are used for the velocities at a solid wall. A periodic solver by Napolitano (1985) was used to relax the discretized equations upstream and downstream of the blade profiles.

The boundary condition required to solve the pressure equation is that the normal derivative of the pressure vanishes at the solid boundary in the computational plane. The actual pressure value at the blade profile is determined by extrapolating from the interior nodes to the wall with the condition of zero normal derivative of the pressure.

On the blade surfaces, both the turbulent kinetic energy (k) and the normal derivative of the dissipation rate (ϵ) were set equal to zero, as recommended by Patel et al. (1984).

RESULTS AND DISCUSSION

A detailed numerical investigation has been conducted for a cascade geometry, in which results calculated by the above PSM have been compared with the available experimental data. The PSM has been validated and compared to the PCM for various complex flows by Hobson and Lakshminarayana (1989).

Double Circular Arc Cascade:

-1.5 Degrees Incidence

For the test case of turbulent flow through a cascade, the predictions made by the present method were compared with the experimental data obtained by Deutsch and Zierke (1986) and Zierke and Deutsch (1989). The blade section is a double circular arc with a camber of 65 degrees and a chord of 228.6 mm, with a leading and trailing edge radius of 9.14 μm. The solidity of the cascade was 2.14, the stagger angle was 20.5 degrees, and the aspect ratio was 1.61. The measurements were made at a chord Reynolds number based on the inlet absolute flow velocity of 5.0×10^5 (with air as the test medium) and at three different incidence angles, +5.0 degrees, -1.5 degrees and -8.0 degrees. The computed test case was for the near design case of -1.5 degrees incidence.

The modified version of the GRAPE code, written by Sorenson (1981), was used to generate the H-grid which extended half a chord upstream and one and a half chords downstream of the blade. The inlet angle of the grid was aligned with the incoming flow at 51.5 degrees and the outlet grid angle was set equal to the measured outlet flow angle of 2.1 degrees. Typical Navier-Stokes calculations using a 130 streamwise by 100 tangential computational grid took 300 outer iterations to decrease the residuals by two orders of magnitude. A typical convergence history, Fig. 2, shows the sum of the L_2 norm of the errors for the complete flowfield at each iteration. The top, middle and bottom curves are the norms for the u-momentum, v-momentum, and pressure equations respectively. For the loss versus incidence prediction, it is felt that two orders of magnitude reduction of the errors is adequate for engineering accuracy. However, for the -1.5 degrees incidence case, the residuals were reduced by four orders of magnitude in roughly 2000 iterations. This corresponded to 20 minutes on the ETA-10 supercomputer, using only the optimization capabilities of the compiler which vectorizes inner DO-loops. The slope of the convergence plots were not monotonic and flattened out after 300 iterations.

Although an inlet freestream turbulence intensity (Tu) of .18% was quoted in the original paper by Deutsch and Zierke (1986), this was measured in the wind tunnel without the cascade in place. A value of freestream turbulence intensity of 2% was used, after consultation with Zierke (1989), with an associated length scale, L_i, of 1mm (L_i/CHORD = 0.004). This gives the inlet turbulent kinetic energy, k_i, as

$$k_i = 1.5(U_i Tu)^2 \qquad [35]$$

Where U_i is the inlet freestream velocity. The high inlet freestream turbulence intensity is due to the flow distortion caused by the cascade resulting in a production of turbulence. Following Rodi and Scheuerer (1985), the inlet turbulent dissipation rate ϵ_i is calculated from the following:

$$\epsilon_i = \frac{k_i^{3/2}}{L_i} \qquad [36]$$

Fig. 3 shows a comparison of the calculated and measured static pressure distribution. The pressure surface has a large favorable pressure gradient near the leading edge. The distribution is flat over most of the rest of the blade, and becomes favorable once again at the trailing edge. The suction surface has a large adverse pressure gradient near the leading edge, followed by a mild favorable gradient between 4% and 10% chord. The code was not able to capture the pressure spike exactly at the leading edge, but was able to follow the distribution after the leading edge closely. Zierke and Deutsch (1989) note that the very large adverse pressure gradient at the leading edge of the suction surface implies a leading edge separation bubble. No evidence of leading edge separation was predicted by the code. The adverse pressure gradient over the rest of the suction surface is computed and the final vanishing adverse pressure gradient near 80% chord is also predicted with the code. The experimental measurements indicated a possible separation region near the trailing edge. Surface flow visualization tests using the chemical sublimation method showed, with a 95% confidence level, a region of low shear stress at 45.1% ±2.3% chord.

Suction Surface Boundary Layers. Suction surface boundary layer profiles were measured by Zierke and Deutsch (1989) with a single component TSI laser Doppler velocimeter (LDV) at 11 chordwise locations. Fig. 4 shows the comparison of the predicted and experimental data for three of the chord locations. The three locations are at 19.7%, 48.9% and 90.2% chord. Good agreement is achieved over most of the blade profile where the boundary layer remains

attached. Both the freestream velocities and the boundary layer profiles are predicted accurately.

The velocity profile is not accurately predicted in the separated region. Liu et al. (1988) computed the same cascade test case, but at 5.0 degrees incidence. They used the Baldwin-Lomax (1978) turbulence model, which did not predict any flow separation, and the two-equation (k-ϵ) model introduced by Launder and Spalding (1974), which predicted flow separation at 90% chord. The present computations show too large a reverse flow, and there is subsequently not enough diffusion, thus resulting in the overall growth of the boundary layer being suppressed. The reason postulated for the failure of the turbulence model to predict separated flow is that the values of k, ϵ and thus μ_t are excessively damped in the recirculating region, as the turbulent Reynolds numbers, Re_y and Re_t, are too small in the reverse flow region. The eddy viscosity model based on k and ϵ cannot account for the anisotropy of the turbulence due to streamline curvature in the separated region.

The prediction of detachment of the flow from the suction surface is in good agreement with the flow visualization measurements. The code computed the onset of separation to be at 50% chord, which agrees well with the 45.1% measured.

The behavior of the turbulence quantities, such as the turbulent kinetic energy and dissipation on the suction surface, are of interest. Distributions of turbulence intensity (Tu) through the suction surface boundary layer at the three chordwise locations considered earlier are presented in Fig. 5 a, b and c. Close to the leading edge (Fig. 5a), where the comparison with the experimental data is good, the turbulence is a maximum close to the wall. The boundary conditions at the solid wall are that k goes to zero and along the blade surface the first grid point was always within a $y^+ < 3.0$ away from the wall. The predicted maximum value for turbulence intensity moves away from the wall as the boundary layer develops over the suction surface (Fig. 5b). However, the experimental data shows that the maximum value was still close to the wall. In the separated flow region (Fig. 5c) the position of the maximum value is 30% closer to the wall than the measured maximum turbulence intensity. This is one of the possible explanations why the boundary layer growth in the separation bubble is under-predicted. The turbulence model is able to predict the increase of turbulent kinetic energy due to streamwise diffusion effects that take place as the boundary layer separates between 49.8% and 90.2% chord. The freestream turbulence intensity at the edge of the boundary layer is predicted well for both 19.7% and 49.8% chord, and over-predicted in the separated region.

Pressure Surface Boundary Layers. Pressure surface boundary layer profiles were measured at 12 locations. Fig. 6 shows the comparison of the predicted and experimental data for the three chord locations on the pressure surface. The locations are at 20.5%, 49.7% and 89.7% chord. Excellent agreement is achieved over the front portion of the blade. The analysis of the experimental data by Zierke and Deutsch (1989) showed that the boundary layer experiences transition from 55.1% chord to 70.3% chord. The agreement at mid chord is acceptable; however, the turbulence model seems to over-predict the transitional boundary layer. Close to the trailing edge where the boundary layer is fully turbulent, a good agreement is once again achieved.

Prediction of Skin Friction. The comparison of the blade surface skin friction distribution is presented in Fig. 7. Transition of the pressure surface boundary layer from laminar to turbulent flow is predicted by this technique. The onset of transition is predicted to be at 10% chord, which is early in comparison to the experimentally determined transition process. Transition seems to be complete by 30% chord; thus, the length of the transitional region is in agreement with that which is determined experimentally. The experimental points were determined by fitting a spline through the measured boundary layer profiles. The level of skin friction coefficient in the fully turbulent region is accurately predicted, as well as the final increase at the trailing edge. Good agreement is achieved between the predicted and experimental skin friction coefficient on the suction surface of the blade. Shown on this figure is the separation point as determined by the flow visualization technique, and the separation point as predicted by the code with good agreement. The levels of skin friction are very close to zero over most of the rear part of the blade.

Leading and Trailing Edge Flows. A complete flowfield with, velocity vector plot, is presented in Fig. 8 a, and details are shown for the leading edge (Fig. 8 b) and trailing edge flows (Fig. 8 c). The separated flow region is clearly visible over the rear part of the suction surface.

Even though the incidence angle was set at -1.5 degrees at a distance of half a chord upstream of the cascade, the angle of attack at the leading edge is positive. This angle was locally determined to be equal to 5.5 degrees, which is rather high. The code is able to capture the upstream influence of the cascade on the flow and in particular the effect on the stagnation streamline. Flow reversal is predicted around the rounded leading edge from the stagnation point over to the suction surface. On the suction surface, the onset of a leading edge separation bubble is evident; however, as stated earlier, the code did not predict any flow reversal.

The trailing edge flow region is most interesting from a microscopic viewpoint. Firstly, as is shown, the separated flow reattaches to the suction surface right at the trailing edge at 99% chord. Thus, the flow leaves the trailing edge in the same direction from both surfaces. No unsteady trailing edge vortices are shed, as would be the case if the separation bubble were not to reattach. This leads to a steady solution computationally. However, the code still needs to deal with the unsteady separated region which has now moved into the freestream. Secondly, the trailing edge wake is immediately "washed out" by the flow in that region, and the only wake evident is that due to the detached separation region. The high shear generated by the flow differential from pressure-to-suction side at the trailing edge is the cause of sudden decay of the trailing edge wake. This is analogous to a jet-wake flow, with the pressure side flow being the jet flow, and the suction side separation the wake flow.

Wake Profiles. LDV measurements of the near wakes were made at 6% chord and 9.7% chord downstream of the trailing edge, while five-hole probe measurements of the far wake were made at 31.7% chord downstream of the trailing edge. Fig. 9 shows the comparison between the prediction and experimentally measured data for the wake profile at the three measurement locations. Although the overall wake profile is not well predicted, some features are well simulated in this complex flow region where the separated flow and the wake interact. The amount of reverse flow at the wake center is captured, as well as the pressure side profile. The greatest discrepancy, on the suction side near the trailing edge, is due to the inability of the code and the turbulence model in particular to capture the growth of the separated boundary layer.

More accurate predictions of the far wake are computed. The symmetry of the far wake as well as the trajectory of the wake centerline is captured, and the overall defect is predicted within engineering accuracy.

The predicted loss coefficient, 0.084, for this profile compares within 10% of 0.094, which was determined from the experimental data. The tangential location of the wake is reasonably predicted. The wake centerline trajectory is captured well, considering the complexity of the flow with intense mixing between the separated flow on the suction side and the pressure side boundary layer. The far wake location is off by only 5 mm from the measured value.

Double Circular Arc Cascade:
Variable Incidence Study

Turning now to the overall prediction of cascade performance with the Navier-Stokes technique, the computation of the above test case was performed at various incidence angles. Zierke and Deutsch (1989) have tested the DCA cascade at -8.5, -1.5 and 5.0 degree angles of incidence. From α=-1.5 to α=5.0 degrees, the C_L vs α curve displays the classical behavior of an airfoil at increasing angles of attack. The lift coefficient for the high negative incidence case is surprisingly higher than the positive incidence case, which seems to suggest that the flowfield is significantly effected by the laminar separation bubble that forms on the pressure surface at the leading edge.

The code was used to predict the global flow parameters for -1.5 and 5.0 degrees incidence. Table 1. shows the comparison between the lift coefficient determined from the experimentally measured blade surface pressure distribution and the computed pressure distribution.

Table 1. Comparison Between the Measured and Computed Lift Coefficient

α	C_L		% Error
(Deg)	Experiment	Computed	
-1.5	0.821	0.846	3.05
5.0	0.952	1.009	5.99

Over the incidence range considered, the accuracy of the prediction is within 6% of the measured values.

Table 2. Comparison Between the Measured and Computed Loss Coefficient

α	$\bar{\omega}$		% Error
(Deg)	Experiment	Computed	
-1.5	0.094	0.084	10.64
5.0	0.151	0.139	7.95

Similarly, the loss predictions are good for the two incidences considering the complex viscous and turbulent dissipation mechanisms in the blade boundary layers. The consistent under-prediction of the loss coefficient is due the inability of the turbulence model to accurately capture the growth of the separation bubble on the rear part of the suction surface.

Table 3. Comparison Between the Measured and Computed Deviation Angle

α	δ (eg)		% Error
(Deg)	Experiment	Computed	
-1.5	14.1	13.5	5.25
5.0	16.0	14.4	10.13

The errors in the prediction of the outlet deviation angle, as shown in Table 3., are comparable to the errors for the lift prediction. These errors are within the experimental accuracy of the measurements.

Variation of Inlet Turbulence Intensity

Having achieved confidence in the code, an attempt was made to understand the effect of inlet freestream turbulence intensity on the cascade performance. A parametric study was carried out by varying the turbulence intensity level; the turbulence length scale was kept constant. At the high incidence angle case (α=5.0 degrees) the inlet freestream turbulence intensity was increased to 4% and 8% respectively. The effect of this increase on the blade loading was computationally studied. Fig. 10 shows the pressure distribution for varying turbulence intensity. Although the overall lift coefficient did not vary by more than 2%, an interesting result is evident in the increase of the exit static pressure. This results in a decrease in the total pressure loss coefficient through the cascade of 14% (ω=0.119) for the 4% turbulence case and 18% (ω=0.114) for the 8% turbulence case. The decrease in total pressure loss coefficient which is computed has also been experimentally measured by Evans (1972).

Fig. 11 shows the effect of increasing turbulence intensity on the blade surface skin friction. Although the distribution of blade surface skin friction coefficient is increased for increasing turbulence levels, this merely indicates that the boundary layers are decreasing in thickness. The increase in turbulence from 2% to 4% caused the suction surface boundary layer to remain attached over the complete length of the blade. The 5.0 degrees incidence case at 2% inlet turbulence intensity showed suction surface boundary layer separation at 55% chord, and this was experimentally determined by Deutsch and Zierke (1986) to occur at 60% chord. This result is consistent with that reported by Schlichting and Das (1963). They showed that the influence of the increase in turbulence level decreased the loss coefficient substantially over the Reynolds number range of $0.5\text{-}5.0\text{x}10^5$, with the major contribution to the decrease in loss coefficient being the elimination of the separation of the suction surface boundary layer.

On the pressure surface, the effect on the skin friction distribution was most effective when the turbulence levels were increased from 2% to 4%. The increase in turbulence level from 4% to 8% decreased the boundary layers on both surfaces, and thus only a small decrease in the loss coefficient was computed.

CONCLUSION

A new technique for computing viscous incompressible flowfields is presented and validated for cascades. The present method permits computation on a regular grid instead of on a staggered grid and allows for the solution of the pressure and not the pressure correction. In most test cases, this procedure showed better convergence behavior than the original pressure correction method. The method closely couples the velocity and pressure field, and thus does not suffer from pressure oscillations.

For complex flow situations such as a separated compressor cascade, the code exhibits satisfactory convergence behavior.

The global parameters such as pressure distribution, lift coefficient and losses are well predicted within engineering accuracy.

The agreement between the computed and measured boundary layer profiles for attached flows on both blade surfaces is very good.

Separated flow predictions need to be further investigated, most probably with higher order turbulence models that take into account the streamline curvature and anisotropy of the turbulence in the separated region.

Details of the leading edge flow and particularly the reattachment of the separated trailing edge flow on the suction surface have been resolved, which shed more light on these complex flow regions.

The code has predicted the cascade performance over a moderate incidence range; however, the minimum loss or high negative incidence test case still needs to be computed.

The effect of increasing the freestream turbulence intensity has been investigated. At high positive incidence the flow separation was inhibited when the turbulence intensity was increased resulting in a decrease in the total pressure loss coefficient.

For flow over complex geometries with pressure gradients or separation, the minimum turbulence model that must be used is the Low-Reynolds-Number k-ϵ model. Its ability to predict transition dependent on freestream turbulence intensity is well known, and it was used in the present study to predict separated flow.

ACKNOWLEDGEMENTS

The authors wish to acknowledge the John von Neumann Supercomputer Center (Princeton) for providing computational time under grant NAC 817, and for partial support from the National Aeronautics and Space Administration through the grant NSG 3266 with P. Sockol as the grant monitor.

REFERENCES

Abdallah, S. (1989) Private Communication.

Baldwin, B. S. and Lomax, H. (1978), "Thin Layer Approximation and Algebraic Model for Separated Turbulent Flows," AIAA paper 78-257.

Caretto, L. S., Gossman, A. D., Patankar, S. V. and Spalding, D. B. (1972), "Two Calculation Procedures for Steady Three Dimensional Flows with Recirculation," *Proc. Third International Conference on Numerical Methods in Fluid Dynamics*. Springer-Verlag, pp. 60-68.

Davis, R. L., Hobbs, D. E. and Weingold, H. D. (1988), "Prediction of Cascade Performance Using a Navier-Stokes Technique," Transactions of the ASME, *Journal of Turbomachinery*, Vol. 110, pp. 520-531.

Deutsch, S. and Zierke, W. C. (1986), "The Measurement of Boundary Layers on a Compressor Blade in a Cascade at High Positive Incidence Angle, Part I Experimental Techniques and Results," NASA CR 179491.

Deutsch, S. and Zierke, W. C. (1986), "The Measurement of Boundary Layers on a Compressor Blade in a Cascade at High Positive Incidence Angle, Part II Data Report," NASA CR 179492.

Evans, R. L. (1972), "The Effect of Freestream Turbulence on the Profile Boundary Layer and Losses in a Compressor Cascade," Aeronautical Research Council, (U.K.) 1282.

Hah, C. (1984), "A Navier-Stokes Analysis of Three-Dimensional Turbulent Flows Inside Turbine Blade Rows at Design and Off-Design Conditions," ASME *J. Eng. Power*, Vol 106, pp. 421-429.

Hobson, G. V. and Lakshminarayana, B. (1989), "Fully Elliptic Incompressible Flow Calculations on Regular Grid by a New Pressure Substitution Method," AIAA paper 90-0239, To be presented at the 28th Aerospace Sciences Meeting, Reno, Nevada.

Lam, C. K. G. and Bremhorst, K. (1981), "A Modified Form of the k-ϵ Model for Predicting Wall Turbulence," *Journal of Fluids Eng.* Vol. 103, pp. 456-460.

Launder, B. E. and Spalding, D. B. (1974), "The Numerical Computation of Turbulent Flows," *Computer Methods In Applied Mechanics and Engineering*. pp. 269-289.

Liu, J., Sockol, P. M. and Prahl, J. M. (1988), "Navier-Stokes Cascade Analysis with a Stiff k-ϵ Turbulence Solver," AIAA-88-0594, Presented at the 26th Aerospace Sciences Meeting, Reno, Nevada.

Napolitano, M. (1985), "A Fortran Subroutine for the Solution of Periodic Block-Tridiagonal Systems," *Communications in Applied Numerical Methods*. Vol. 1, pp. 11-15.

Patel, V. C., Rodi, W. and Scheuerer, G. (1985), "A Review and Evaluation of Turbulence Models for Near Wall and Low Reynolds Number Flows," AIAA *Journal*, Vol. 23, pp. 1308-1319.

Pouagare, M. and Lakshminarayana, B. (1986), "A Space-Marching Method for Viscous Incompressible Internal Flows," *J. Comp. Physics*. Vol. 64, No. 2, pp. 389-415.

Rhie, C. M. and Chow, W. L. (1983), "Numerical Study of the Turbulent Flow Past an Airfoil with Trailing Edge Separation," AIAA *Journal*, Vol.21, pp. 1525-1532.

Rodi, W. and Scheuerer, G. (1985), "Calculation of Heat Transfer to Convection-Cooled Gas Turbine Blades," *Journal of Eng. for Power*, Vol. 107, pp. 620-627.

Schlichting, H. and Das, A. (1963), "Recent Research on Cascade Flow Problems," DFL-Bericht Nr. 202, Braunschweig.

Shih, T. M. and Ren, A. L. (1984), "Primitive Variable Formulations Using Nonstaggered Grids," *Numerical Heat Transfer*, Vol. 7. pp. 413-428.

Sorenson, R. L. (1981), "A Computer Program to Generate Two-Dimensional Grids About Airfoils and Other Shapes by the Use of Poisson's Equation," NASA Technical Memorandum 81198.

Spalding, D. B. (1972), "A Novel Finite Difference Formulation for Differential Expressions Involving Both First and Second Derivatives," *Int. Journal for Numerical Methods in Engineering*, Vol. 4, pp. 551-559.

Zierke, W. C. and Deutsch, S. (1989), "The Measurement of Boundary Layers on a Compressor Blade in Cascade: Part 4-Flow Fields for Incidence Angles of -1.5 and -8.5 Degrees," ASME 89-GT-72. (To be published in the *J. Turbomachinery*)

Zierke, W. C. (1989), Private Communication.

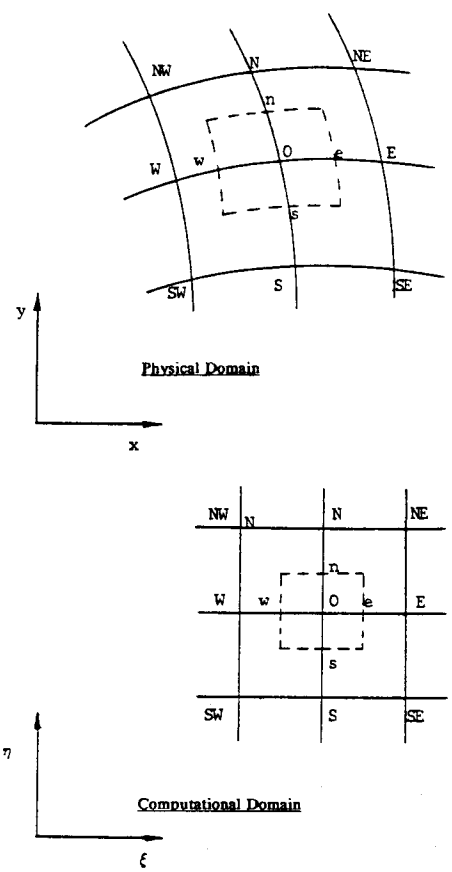

Fig. 1. Schematic Representation of a Control Volume in Physical and Computational Space

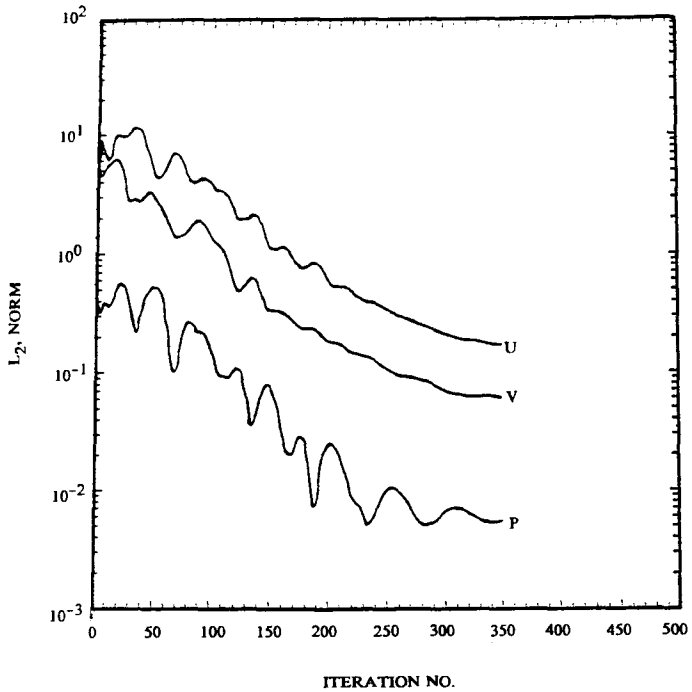

Fig. 2. Convergence History for Turbulent Flow in a Double Circular Arc Cascade

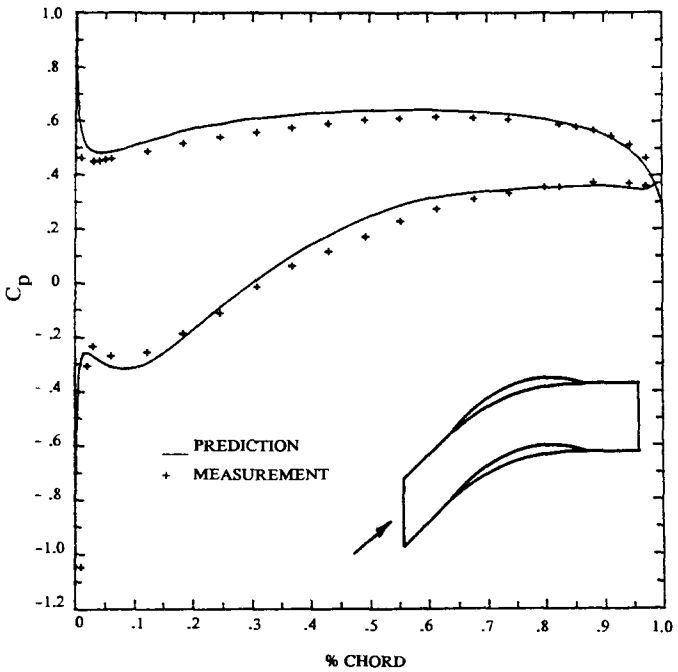

Fig. 3 Predicted and Measured Blade Surface Pressure Coefficient

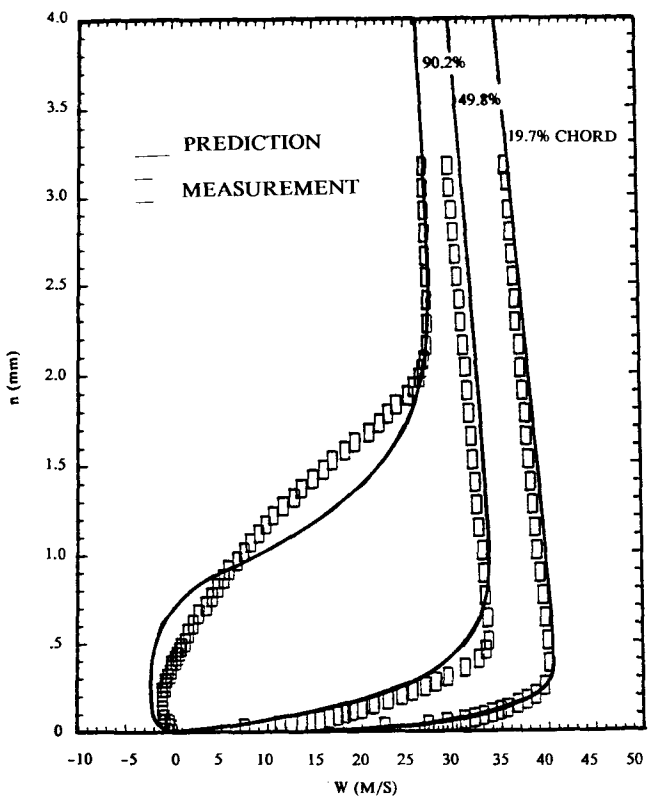

Fig. 4 Comparison of the Computed and Measured Velocity Distribution on the Suction Surface

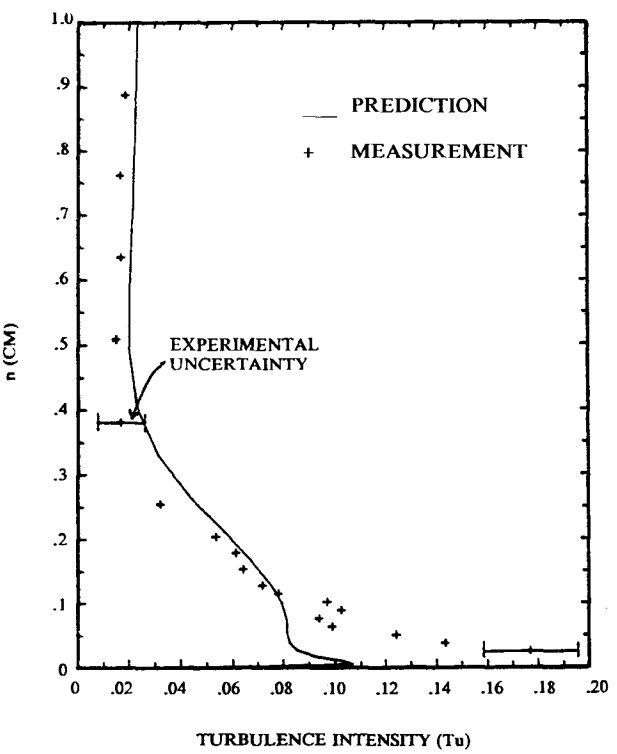

Fig. 5a Comparison of the Computed and Measured Turbulence Intensity on the Suction Surface: 19.7% Chord

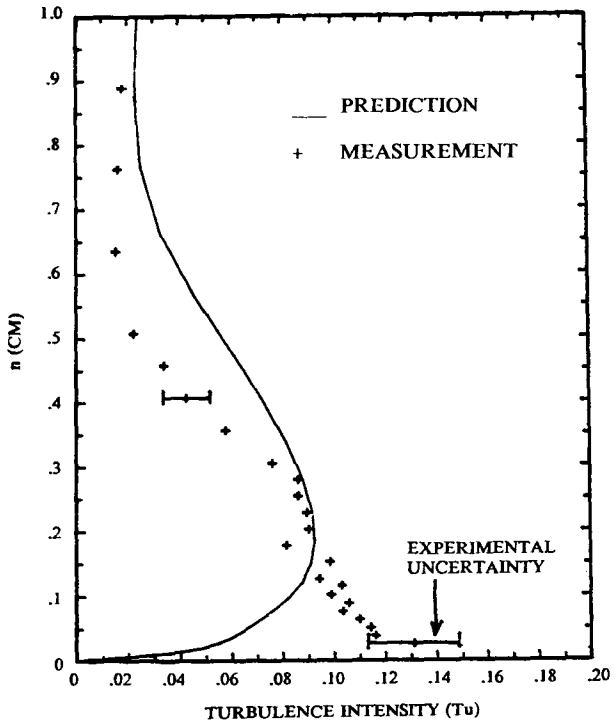

Fig. 5b Comparison of the Computed and Measured Turbulence Intensity on the Suction Surface: 49.8% Chord

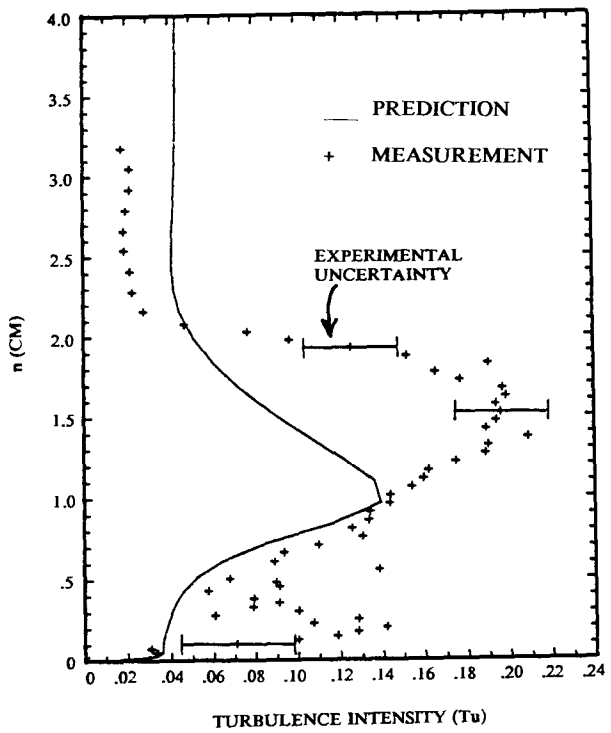

Fig. 5c Comparison of the Computed and Measured Turbulence Intensity on the Suction Surface: 90.3% Chord

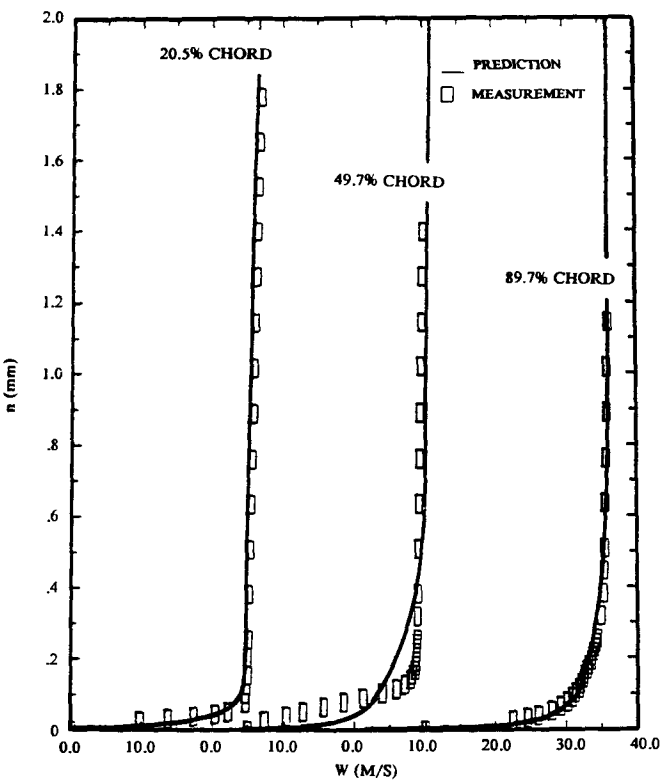

Fig. 6 Comparison of the Computed and Measured Velocity Distribution on the Pressure Surface

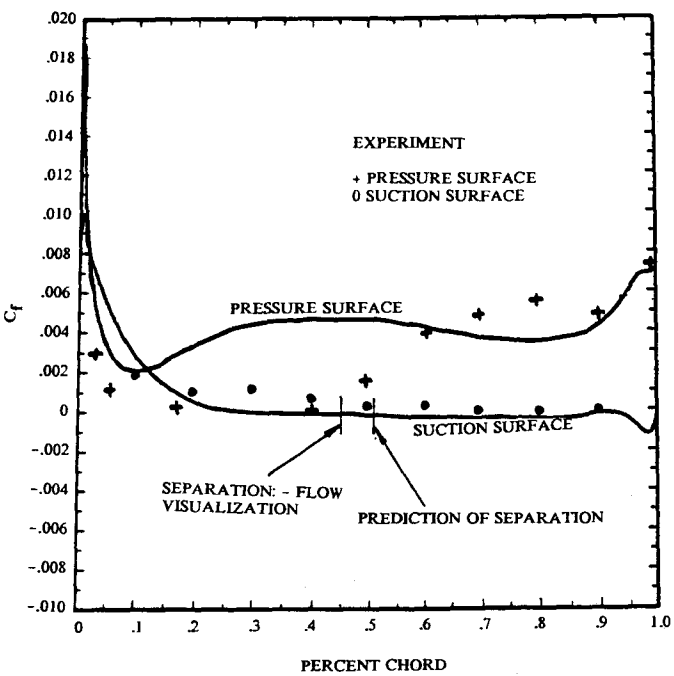

Fig. 7 Comparison of the Computed and Measured Skin Friction Coefficient on the Blade Surface

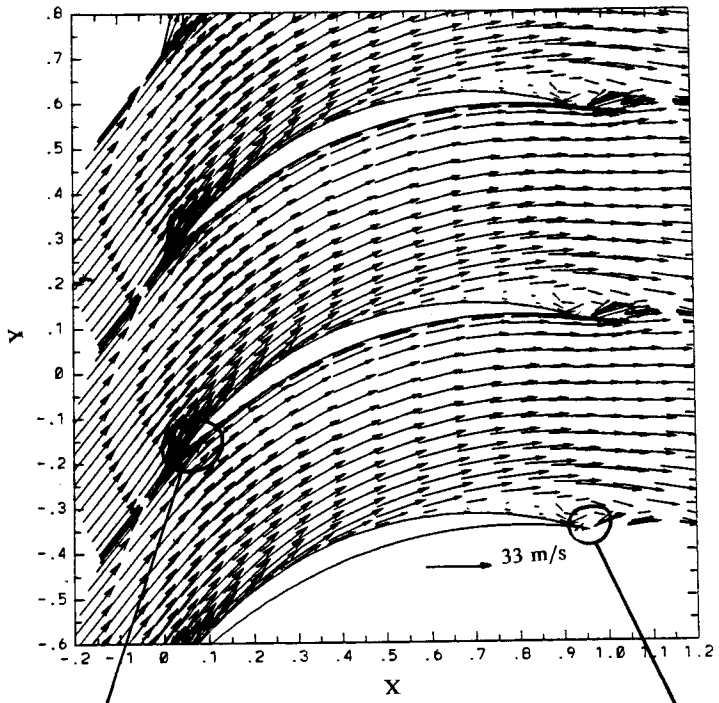

Fig. 8a Velocity Vector Distribution Through the Double Circular Arc Cascade; -1.5 Degrees Incidence

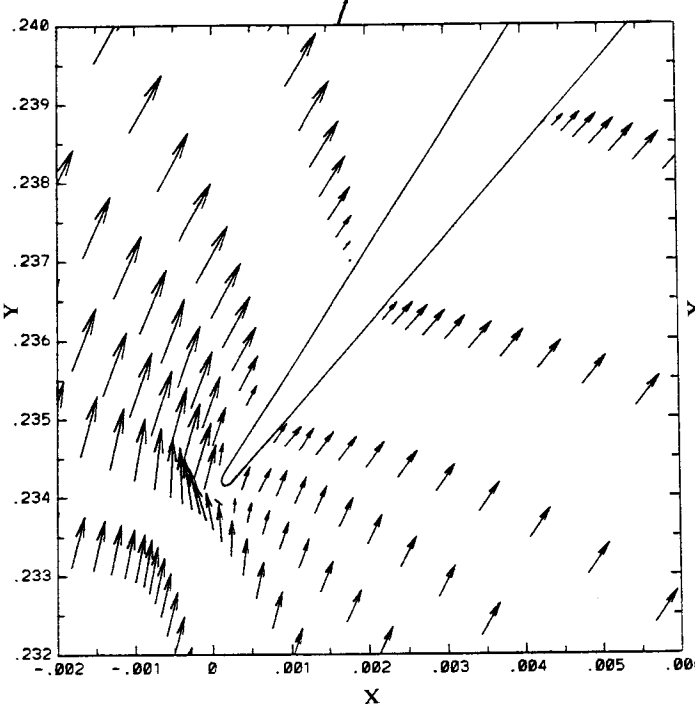

Fig. 8b Detail of Leading Edge Flow

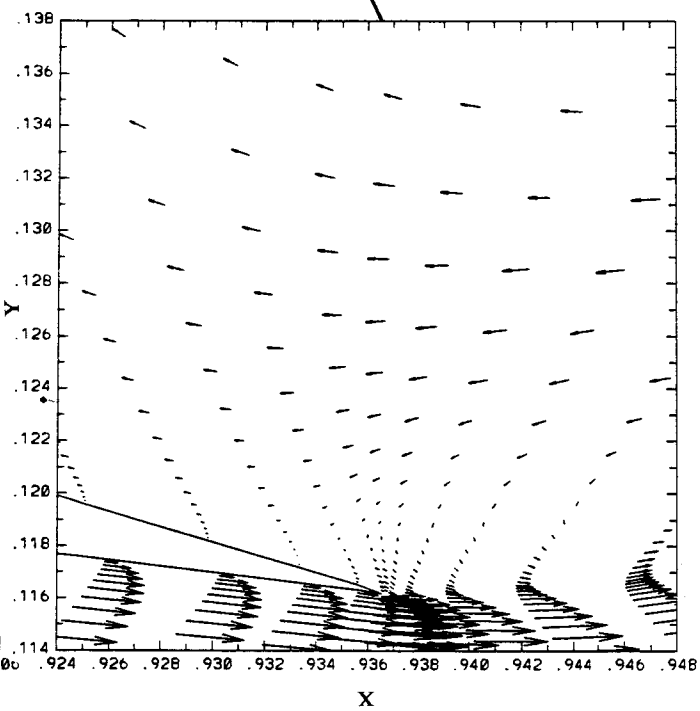

Fig. 8c Detail of Trailing Edge Flow

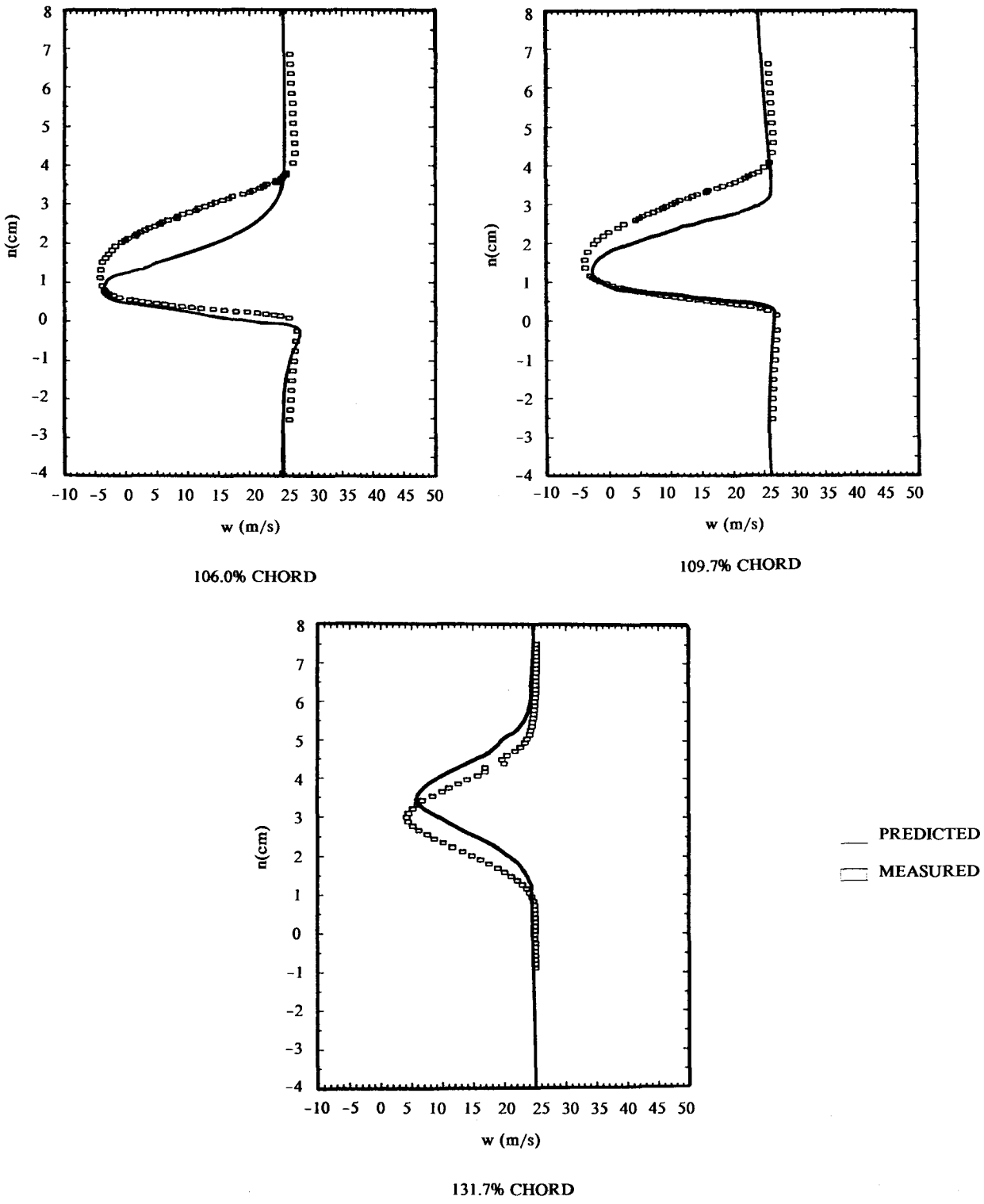

Fig. 9 Comparison of Computed and Measured Axial Velocity Distribution in the Wake

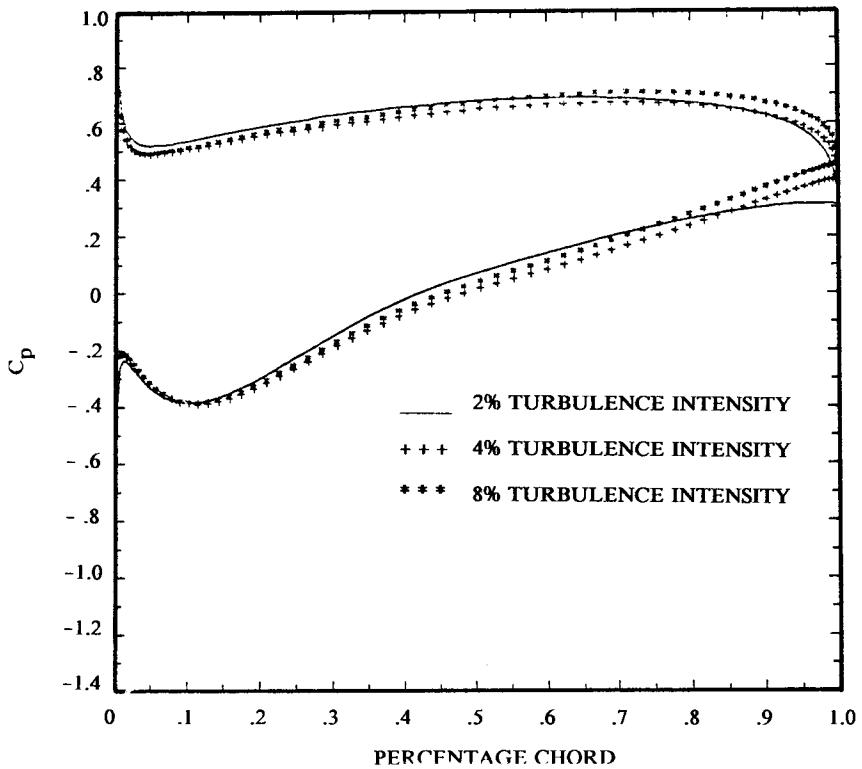

Fig. 10 Effect of Increasing Turbulence Intensity on the Distribution of Static Pressure Coefficient

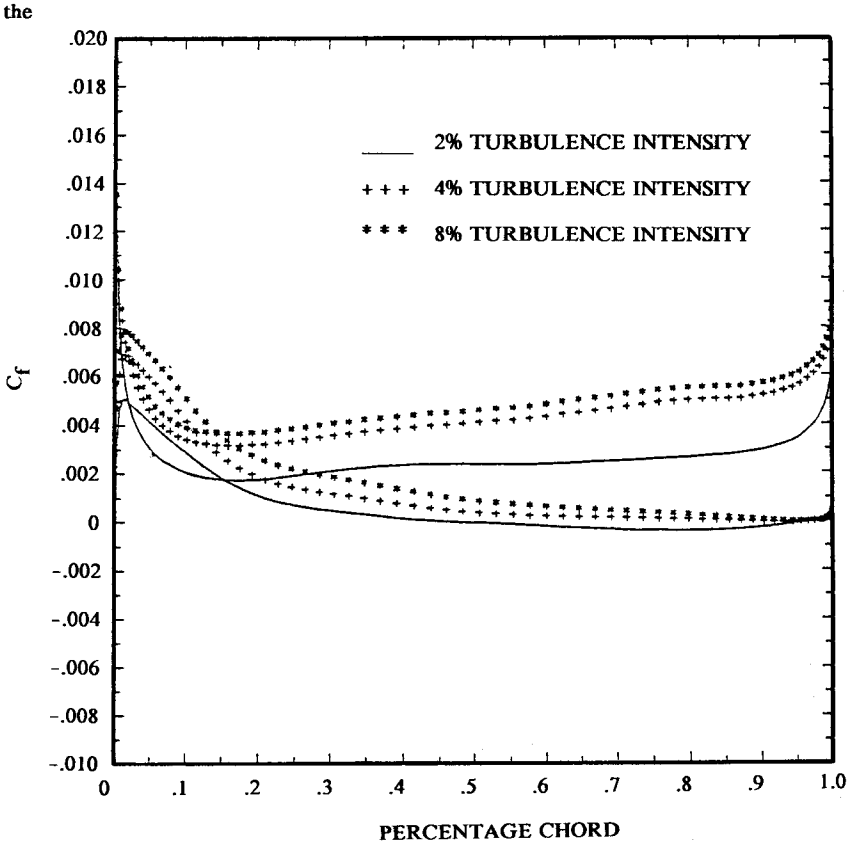

Fig. 11 Effect of Increasing Turbulence Intensity on the Distribution of Blade Skin Friction Coefficient